

Two-photon photoassociation spectroscopy of the $^2\Sigma^+$ YbLi molecular ground state

Alaina Green,^{1,*} Jun Hui See Toh,¹ Richard Roy,¹ Ming Li,² Svetlana Kotochigova,² and Subhadeep Gupta¹

¹*Department of Physics, University of Washington, Seattle, Washington 98195, USA*

²*Department of Physics, Temple University, Philadelphia, Pennsylvania 19122, USA*

(Dated: March 27, 2022)

We report on measurements of the binding energies of several weakly bound vibrational states of the paramagnetic $^{174}\text{Yb}^6\text{Li}$ molecule in the electronic ground state using two-photon spectroscopy in an ultracold atomic mixture confined in an optical dipole trap. We theoretically analyze the experimental spectrum to obtain an accurate description of the long-range potential of the ground state molecule. Based on the measured binding energies, we arrive at an improved value of the interspecies s -wave scattering length $a_{s0} = 30 a_0$. Employing coherent two-photon spectroscopy we also observe the creation of “dark” atom-molecule superposition states in the heteronuclear Yb-Li system. This work is an important step towards the efficient production of ultracold YbLi molecules via association from an ultracold atomic mixture.

I. INTRODUCTION

Ultracold molecules expand the scientific reach of ultracold atoms through their richer internal structure. Samples of ultracold polar molecules are sought for their tunable long-range interactions which form the basis for studies of strongly correlated many-body systems as well as serving as building blocks for quantum information processing [1, 2]. Precision spectroscopies on ultracold molecules can be used to search for time variations of fundamental constants [3–5] and test fundamental symmetries [6–8]. To reach the high phase space densities (PSD) required for several of these proposed applications of ultracold molecules, an established strategy is to coherently transform pairs of atoms from within high PSD atomic mixtures into a sample of ultracold ground state molecules through a sequence of magneto-association and Stimulated Raman Adiabatic Passage (StiRAP) processes [9–14].

While this strategy has been successful so far only in bi-alkali atom pairs, there is general interest in extending it to other diatomic systems such as dimers containing one alkaline-earth-like and one alkali atom (e.g. YbLi), which are attractive due to the new degree of freedom from the unpaired electron. While this difference in electronic structure make magneto-association more challenging in these systems [15–17], several groups are actively pursuing this experimental front [18–21]. The resulting combination of electric and magnetic dipole moments in the molecular ground state are appealing properties for their proposed use towards quantum simulation of spin lattice models and studies of symmetry-protected topological phases, spin liquids, and quantum magnetism [2, 22]. The $^2\Sigma^+$ ground state of such molecules also make them promising candidates for fundamental symmetry tests as well as ultracold chemistry with a spin degree of freedom [1, 2].

In this paper, we report on first measurements probing

bound states of the $^{174}\text{Yb}^6\text{Li}$ $^2\Sigma^+$ ground state molecule by two-photon photoassociation (PA) spectroscopy. We observe several weakly bound states constituting a single vibrational spectrum, which we theoretically analyze to accurately determine the long-range dispersion coefficients for this potential. Our analysis also yields an improved value of the YbLi ground state s -wave scattering length. Through coherent two-photon spectroscopy, we also observe “dark” atom-molecule superposition states and perform a precise measurement of the least-bound vibrational state energy. Our results are an important step towards efficient coherent production of YbLi molecules via association from ultracold atoms.

The rest of this paper is organized in the following way. In Section II, we describe our experimental method and results for the determination of vibrational states in YbLi using PA spectroscopy. In Section III, we describe our theoretical analysis of the observed spectrum and determination of the long-range molecular potential, and in Section IV we discuss the resulting value for the ground state s -wave scattering length. We present our observation of atom-molecule superposition states in Section V and provide a summary and outlook in Section VI.

II. TWO-PHOTON SPECTROSCOPY

A. Experimental strategy

The schematic for the PA process is shown in Figure 1. Within a trapped mixture of ultracold atoms, a Li and Yb atom pair is resonantly coupled to an electronically excited molecular state by a free-bound (FB) laser. A bound-bound (BB) laser couples this electronically excited molecule to the electronic ground state. Resonant two-photon coupling is achieved when the energy difference between the BB and FB photons is equal to the binding energy of the ground-state molecule.

We detect resonant coupling to a molecular state by trap-loss spectroscopy. When the atoms are exposed to only the FB laser beam, a one-photon free-bound PA resonance is detected as a frequency-dependent loss of

* agreen13@uw.edu

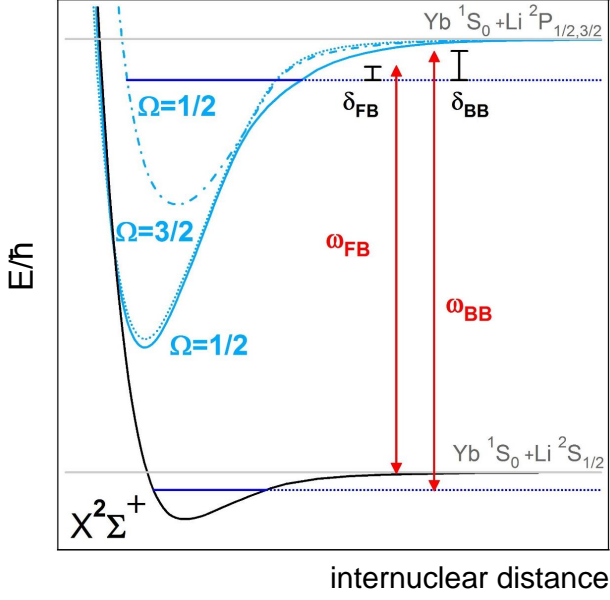


FIG. 1. A schematic representation of two-photon spectroscopy. ω_{FB} and ω_{BB} are the angular frequencies of the free-bound and bound-bound lasers respectively. δ_{FB} and δ_{BB} are the one-photon detunings from the free-bound and bound-bound PA resonances respectively.

atoms from the trap. For two-photon spectroscopy, we stabilize the frequency of the FB laser to a free-bound PA resonance, thus inducing a fixed atom loss from the trap via molecule formation for a fixed exposure time. We monitor this loss in the additional presence of the BB laser beam. As the BB laser frequency is varied, a bound-bound resonance is detected as a suppression of this loss, caused by strong coupling between the excited and ground molecular states which shifts the energy of the excited molecular state and takes the FB laser off the free-bound resonance [23].

In this work we interrogate the least bound states of the YbLi $^2\Sigma^+$ molecular ground potential via an excited molecular state within the Yb(1S_0) + Li(2P) electronic manifold. The intermediate state belongs to a combination of two $\Omega = 1/2$ and an $\Omega = 3/2$ relativistic potentials which asymptotically correspond to the Yb(1S_0) + Li($^2P_{1/2}$) and the Yb(1S_0) + Li($^2P_{3/2}$) thresholds [19]. Ω is the total projection quantum number onto the interatomic axis. Guided by observed favorable free-bound Franck-Condon factors, we induce trap loss through one-photon PA by specifically addressing either the second or the seventh least bound states (labeled $v^* = -2, -7$) within a single vibrational series in the intermediate state [24]. The bound-bound Franck-Condon factors for either of these two intermediate states were high enough to observe the six least-bound vibrational states (labeled $v = -1$ to -6) in the $^2\Sigma^+$ electronic ground state.

B. Experimental setup

Our ^{174}Yb - ^6Li mixture is prepared through a sequence of laser and evaporative cooling techniques using procedures similar to those described in [25]. For the measurements reported in this paper, the atoms are confined in a crossed optical dipole trap with mean harmonic frequency $\bar{\omega}_{\text{Yb(Li)}} = 2\pi \times 492(3936)$ Hz, and with tightest confinement along the vertical direction. Prior to application of PA light, the mixture population of $N_{\text{Yb}} = 2.0 \times 10^6$ in the 1S_0 ground state and $N_{\text{Li}} = 1.4 \times 10^5$ in the $^2S_{1/2}$ $|m_J = -\frac{1}{2}, m_I = -1\rangle$ ground state, has a common temperature of $T = 15 \mu\text{K}$. The clouds are above quantum degeneracy with $T/T_c \simeq 5$ and $T/T_F \simeq 1$, where T_c is the Yb BEC transition temperature and T_F is the Li Fermi temperature. The peak atomic density is $n_{\text{Yb(Li)}} = 2 \times 10^{14} (3.9 \times 10^{13}) \text{cm}^{-3}$.

The PA light is derived from two diode master lasers, each of which is amplified by a tapered amplifier (TA). Using a scanning Fabry-Perot cavity, the frequency of the free-bound laser is actively stabilized relative to an additional laser, itself stabilized to an atomic reference. A wavemeter (High Finesse WS-7) is used to stabilize the frequency of the bound-bound laser. The power in each beam is controlled using independent acousto-optic modulators (AOMs). The two beams are combined and passed through a heated Li vapor cell to suppress frequency components near the Li atomic resonances generated by the TA. The spectrally filtered beams are coupled into a single-mode polarization-maintaining fiber, the output of which is focused onto the trapped atomic mixture with a waist of $75 \mu\text{m}$. This combined beam provided up to 170 W/cm^2 in the FB and 280 W/cm^2 in the BB but the intensities were adjusted for optimum signal, accommodating different Franck-Condon factors. After an exposure time ranging from 10 to 100 ms, the number of atoms remaining in the trap is measured using absorption imaging. A typical 1-photon PA resonance is shown in Fig. 2(a).

The spectroscopic search for heteronuclear YbLi resonances can be hindered by background losses from the trap, notably homonuclear photoassociation of Li_2 [19]. We exploit the fermionic nature of ^6Li to mitigate this background loss by the use of a spin polarized sample at a temperature well below the p -wave barrier of $\sim 8 \text{ mK}$. We perform our spectroscopic search using σ^- PA beam polarizations at a bias field of 420 G. Off-resonant scattering from the PA lasers thus addresses a $m_I + m_J = -\frac{3}{2} \rightarrow -\frac{5}{2}$ cycling transition, preserving the initial spin polarization. The viability of two-photon spectroscopy with such a setup is demonstrated in Fig. 2(b). The loss of atoms when the FB laser is off resonance is sufficiently small compared to the resonant loss to allow for a strong two-photon trap-loss signal. The off-resonant loss is dominated by spontaneous scattering despite nearby Li_2 resonances centered at $2\pi \times 240, 320$ and -220 MHz relative to the $v^* = -2$ YbLi resonance [26].

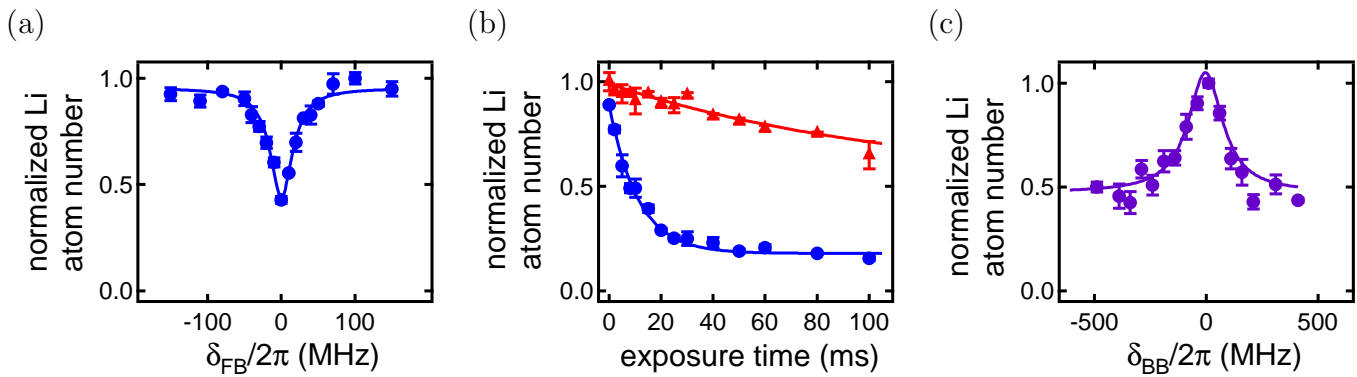


FIG. 2. (a) A representative one-photon PA loss resonance of $v^* = -2$ with a binding energy of 15.9 GHz relative to the Yb $^1S_0 + \text{Li } ^2P_{1/2}$ free atom energy. (b) Evolution of the Li atom number in the presence of resonant (blue circles) and off-resonant (red triangles) PA light. In the resonant case the FB laser is locked to the $v^* = -2$. In the off-resonant case it is locked $2\pi \times 1$ GHz to the red of resonance. (c) A representative two-photon PA resonance of $v = -3$ with binding energy 123.96 GHz relative to the Yb $^1S_0 + \text{Li } ^2S_{1/2}$ free atom energy.

The small reduced mass of YbLi leads to a large vibrational spacing of molecular levels, posing another challenge for the spectroscopic search. Detecting the least-bound vibrational state $v = -1$ required a thorough search over several GHz of spectral range. We utilized the Leroy-Bernstein relation [27] as well as an earlier calculation of the C_6 coefficient for this potential [28] to predict the approximate binding energy of each subsequent state, thus expediting our search. We used this approach to detect weakly bound vibrational states with binding energies extending to greater than 1 THz.

C. Long Range Bound States

A typical two-photon resonance is shown in Figure 2(c). The measured binding energies of the six rovibrational states observed in this way are presented in Table I [29]. The associated error is a combination of PA laser linewidth and wavemeter precision, except for the shallowest state, where a higher precision is achieved through coherent two-photon spectroscopy and is discussed in Section V.

As discussed in Section III, the observed spectrum corresponds to a single vibrational series from $v = -1$ to $v = -6$. In order to verify the magnetic quantum number of these states, we determine the magnetic moment of the $v = -1$ state using two-photon PA spectroscopy at various magnetic fields (see Fig. 3). The magnetic moment is measured to be 1.40(16) MHz/G, equal to that of the initial atom pair state.

To determine the rotational state of the observed levels, we first note that since the experimental temperature is well below the p -wave barrier of ~ 3 mK for the Yb-Li scattering system, we can exclude p -wave and any higher partial wave collisions. This leaves the atoms to interact dominantly through the $l = 0$ s -wave channel. Using the conservation of total angular momentum and parity

along with the fact that the excited intermediate state has an electronic orbital angular momentum $L = 1$, we can conclude that the final rovibrational state after the two-photon PA can only be $l = 0$ or 2. Further identification of the rotational quantum number is realized by fitting the binding energies to a theoretical model, detailed in Section III, which determines that all observed bound states have $l = 0$.

III. THEORETICAL ANALYSIS: GROUND POTENTIAL AND STATE ASSIGNMENTS

A. Ground electronic potential

Ground state $\text{Li}(^2S_{1/2})$ and $\text{Yb}(^1S_0)$ atoms interact through the $X^2\Sigma^+$ Born-Oppenheimer molecular potential. Its weakly bound rovibrational states are particularly sensitive to the long-range part of the potential. We use the Tang-Toennies damped long-range form [30]

$$V(R) = - \sum_{n=3}^5 f_{2n}(R) \frac{C_{2n}}{R^{2n}}, \quad (1)$$

where R is the internuclear separation, $f_{2n}(R)$ is a damping function of the form

$$f_{2n}(R) = 1 - \left(\sum_{k=0}^{2n} \frac{(bR)^k}{k!} \right) e^{-bR}, \quad (2)$$

and b is a fitting parameter that is related to the ionization energies of the two atoms. The leading term of Eq. (1) is defined by the C_6 van der Waals coefficient that has been calculated in our previous work to be 1496(150) $E_h a_0^6$ [28]. It agrees with other theoretical predictions within our uncertainty, *i.e.* 1594 $E_h a_0^6$ from Ref. [31] and [32], and 1551(31) $E_h a_0^6$ from Ref. [33]. Here

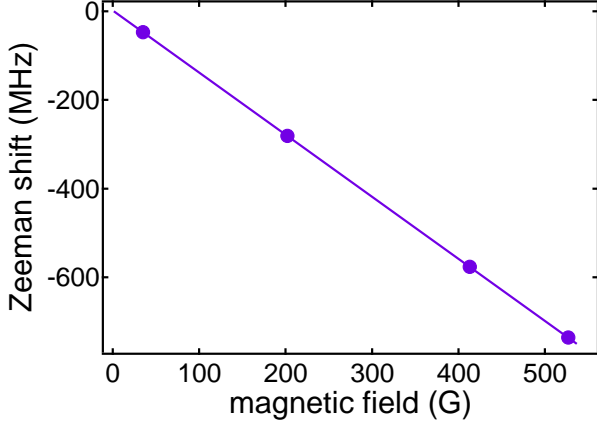


FIG. 3. The magnetic moment of the shallowest bound state of $X^2\Sigma^+$ for $^{174}\text{Yb}^6\text{Li}$ is determined by measuring its binding energy at various magnetic fields using two-photon PA spectroscopy. The Zeeman shift of the molecule is determined by accounting for the Zeeman shift of the initial atomic state.

E_h is the Hartree energy and a_0 is the Bohr radius. The next term is described by the C_8 coefficient which was estimated by Porsev *et al.* to be $1.27(3) \times 10^5 E_h a_0^8$ [34]. We use $C_{10} = (49/40) \times C_8^2 / C_6$ recommended by Thakkar and Smith [35] to reduce the number of fitting parameters. After adjusting the coefficients to fit the measured energies of the weakly bound states, we obtain $C_6 = 1581(5) E_h a_0^6$, $C_8 = 1.49(2) \times 10^5 E_h a_0^8$, and $b = 0.912(9) a_0^{-1}$ (see Section III B). The coefficients are given in atomic units which are abbreviated to a.u. in the following text. Figure 4 shows the fitted long-range potential and the measured energies of the weakly bound states. The precise shape of the short-range part of the potential plays a less significant role in determining the weakly bound state energies. We use a short-range potential that agrees with the average well depth and the general shape of the *ab initio* potentials from [31, 36–38], and smoothly connect it to the long-range part at $14 a_0$.

The depth of the short-range well is adjusted with a Gaussian function

$$g(R) = V_d \times e^{-\frac{(R-R_0)^2}{2c^2}} \quad (3)$$

to facilitate the fitting of the measured energies, where $c^2 = 1.5 a_0^2$ is the minimum of the potential well and V_d is the adjustable parameter for the depth of the potential well at the minimum.

B. Weakly bound rovibrational states

To calculate the energy of a weakly bound state in the ground electronic potential, we use the spinless basis set $|L, m_L\rangle Y_{lm}(\hat{R})$ to expand its wavefunction, where $L = 0$ is the electronic orbital angular momentum with $m_L = 0$ its projection in the laboratory frame, and $Y_{lm}(\hat{R})$ is the spherical harmonic of relative orbital angular momentum

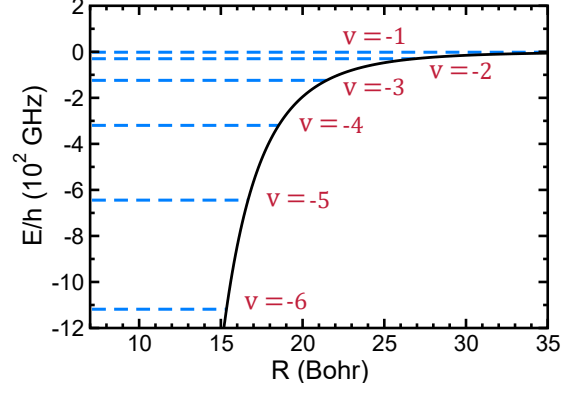


FIG. 4. The long-range shape of the $X^2\Sigma^+$ potential of YbLi and the measured weakly bound rovibrational states labeled by horizontal dashed lines.

TABLE I. Comparisons between the experimentally observed bound state energies and the theory results of $l = 0, 1$, and 2 . h is the Planck constant and the frequencies are given in GHz. The theoretical uncertainties in the last digit are given in parenthesis which are derived from error propagation using the covariance matrix of the four parameters of the potential.

v	exp. E/h	$E_{l=0}^{th}/h$	$E_{l=1}^{th}/h$	$E_{l=2}^{th}/h$
-1	-1.8260(15)	-1.8260(34)	-1.2933(34)	-0.3214(33)
-2	-30.070(26)	-30.100(17)	-28.740(16)	-26.047(14)
-3	-123.957(26)	-124.002(43)	-121.840(40)	-117.533(36)
-4	-319.465(26)	-319.406(45)	-316.470(43)	-310.610(42)
-5	-644.457(26)	-644.484(57)	-640.812(60)	-633.477(64)
-6	-1118.295(26)	-1118.285(60)	-1113.927(59)	-1105.219(58)
-7	-	-1754.07(51)	-1749.08(51)	-1739.10(49)
-8	-	-2546.7(23)	-2541.1(23)	-2530.0(23)

l and its projection m . The unit vector \hat{R} is the direction of the molecular axis in the laboratory frame. The molecular Hamiltonian is then diagonal in this basis set and is the same for different m [39]. We choose $m = 0$ for all our calculations. We use a discrete variable representation (DVR) based method to solve the single channel radial Schrödinger equation numerically for the rovibrational bound state energies of $v = -1$ to -6 . Since the binding energies measured experimentally are the only levels observed for each vibrational quantum number, we cannot directly assign rotational quantum numbers to them. Thus, we vary l from 0 to 2 to serve as an unknown variable in our fitting procedure.

To assign rotational quantum number l_v to the observed states v as well as to find the best fit for the four parameters of the potential including the two dispersion coefficients, the damping function fitting parameter b , and the depth of the short-range potential well V_d , we adopt the following procedure. First, we choose a set of C_6 , C_8 , b , and $l_{v=-1}$, and vary V_d within a range where the total number of bound states remains the same. V_d is varied until the binding energy of the chosen $l_{v=-1}$ state approaches the observed $v = -1$ energy within 1×10^{-5}

GHz. Next, we calculate the bound state energies of $v = -2$ to -6 and $l_v = 0, 1$, and 2 , and for each v we choose among the set of l_v the one closest to the observed energy. For each v , we record the chosen l_v and the energy difference ΔE_v from the observed value. Then we can define χ^2 as

$$\chi^2 = \sum_{v=1}^6 \frac{\Delta E_v^2}{u_v^2}, \quad (4)$$

where u_v is the experimental uncertainty associated with the measured binding energy E_v of the vibrational state v . We also define a total rotation number

$$\lambda = \sum_{v=-1}^{-6} l_v \times 3^{v+6} \quad (5)$$

so that every different set of $\{l_v\}$ corresponds to a unique λ value. In particular, $\lambda = 0$ when all six states have $l_v = 0$.

To minimize χ^2 in a large multidimensional parameter space, we opt to search with coarse step sizes first, then in the vicinity of the minimum we conduct a second search with much finer step sizes. In the first step, we search the C_6 coefficient from 1400 a.u. to 2100 a.u. with a step size of 2 a.u., the C_8 coefficient from 1×10^5 a.u. to 1.8×10^5 a.u. with a step size of 1×10^3 a.u., and the b parameter from 0.7 a.u. to 1.2 a.u. with a step size of 0.005 a.u. χ^2 calculated from the first step is plotted against C_6 and C_8 coefficients in Figure 5a. Parameter b is chosen to minimize χ^2 for each pair of C_6 and C_8 . The color is coded proportional to λ according to the color bar in Figure 5a with $\lambda = 0$ in dark orange. Data points with χ^2 lower than $\sim 10^2$ all corresponds to $\lambda = 0$. The lowest χ^2 is 12.3 that corresponds to $C_6 = 1580$ a.u., $C_8 = 1.49 \times 10^5$ a.u., and $b = 0.910$ a.u. The result of the first step shows that all the experimentally observed bound states correspond to $l = 0$ rotational state.

In the second step, we search the vicinity of the point with minimal χ^2 in the first step with finer step sizes. We vary the C_6 coefficient from 1560 a.u. to 1600 a.u. with a step size of 0.2 a.u., the C_8 coefficient from 1.40×10^5 a.u. to 1.57×10^5 a.u. with a step size of 50 a.u., and the b parameter from 0.88 a.u. to 0.93 a.u. with a step size of 2×10^{-4} a.u. χ^2 calculated from the second step is plotted in Figure 5b. Again, parameter b is chosen to minimize χ^2 for each pair of C_6 and C_8 . The colors of the surface as well as the contours on the 2D grid are coded with the value of χ^2 with lower values approaching red and higher values approaching light blue. All the points shown in the graph corresponds to $\lambda = 0$ which confirms our initial assignment of $l = 0$ for all states. The lowest χ^2 is 10.69 with $C_6 = 1581.0$ a.u., $C_8 = 1.4945 \times 10^5$ a.u., and $b = 0.9116$ a.u. Table I shows the comparisons between the observed energy levels and the calculated ones with the given parameters. The energies predicted for $l = 1$ and 2 as well as $v = -7$ and -8 are also presented.

TABLE II. The uncertainties of and correlation coefficients between the values of the fitted parameters. The uncertainties are the diagonal elements in bold and are in atomic units apart from the one for V_d , which is in cm^{-1} . The dimensionless correlation coefficients are symmetric and defined as $r(x_i, x_j) = u(x_i, x_j)/[u(x_i)u(x_j)]$, where $u(x_i, x_j)$ is the covariance between parameters x_i and x_j and $u(x_{i,j})$ are the uncertainties of parameters x_i and x_j respectively. Only the upper-triangle of the correlation matrix is shown.

	C_6	C_8	b	V_d
C_6	5.18	0.920	0.993	0.973
C_8		1.91×10^3	0.944	0.984
b			8.81×10^{-3}	0.987
V_d				11.52

To analyze the uncertainties of and the correlations between the fitted parameters, we follow the error propagation analysis of Ref. [40]. We have six experimental measurements and four continuous fitting variables [41]. Thus we have two degrees of freedom left. The lowest χ^2 of 10.69 then corresponds to a reduced χ^2 of 5.35 and a Birge ratio R_B of 2.31. Since our Birge ratio is larger than one, we uniformly inflate the experimental uncertainty by the Birge ratio ($u_v \times R_B$). Following the methodology in the Appendix E and F of Ref. [40], we arrive at the uncertainties of and correlation coefficients between the four derived parameters C_6 , C_8 , b , and V_d shown in Table II. The four parameters are highly correlated, indicated by the fact that all the correlation coefficients are close to one.

IV. GROUND STATE S-WAVE SCATTERING LENGTH

Using the fitted potential, we can calculate the zero energy s -wave scattering length a_{s0} numerically. At a finite energy, the s -wave scattering length in single channel scattering is defined as

$$a_s(E) = \frac{1}{ik} \times \frac{1-S}{1+S}, \quad (6)$$

where $k = \sqrt{2\mu E}/\hbar$ is the wavenumber with μ the reduced mass and $\hbar = h/2\pi$ the reduced Planck constant, and S is the complex single channel scattering matrix. The zero energy s -wave scattering length is then $a_{s0} = \lim_{E \rightarrow 0} a_s(E)$. We numerically propagate the single channel radial Schrödinger equation using Gordon's propagator [42], and match the wavefunction at large R to the scattering boundary condition to obtain the S matrix. As a result, the zero energy s -wave scattering length is 30.074(55) a_0 . The uncertainty in the parenthesis is propagated from the variances and covariances of the four potential parameters.

We also calculate the total elastic cross sections

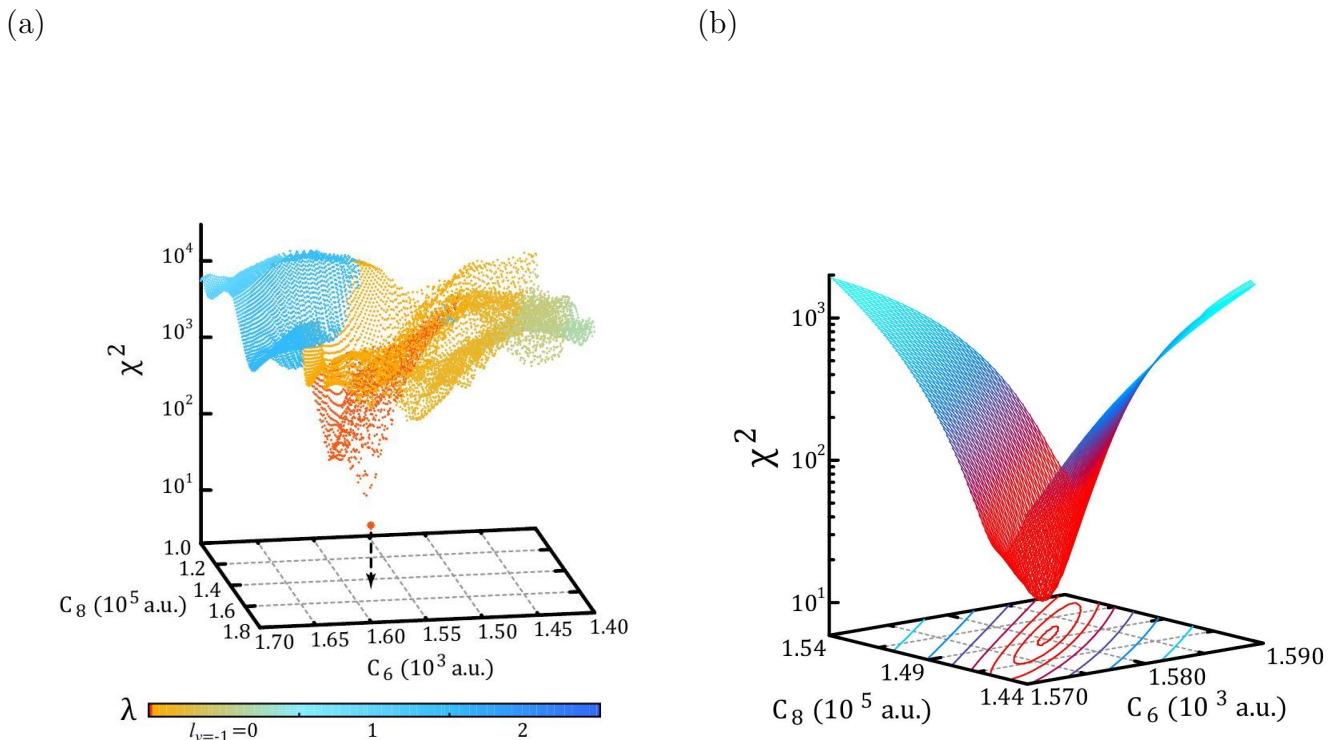


FIG. 5. (color online) χ^2 as a function of the C_6 and C_8 parameters. The rotational quantum number l , the b parameter, and the depth of the potential well are all used to minimize χ^2 for a specific set of C_6 and C_8 . Panel (a) shows the initial search with a coarse grid. The color is coded to the total rotation number λ defined in Eq. (5) according to the color bar. The left side of the color bar corresponds to smaller λ and the right side corresponds to larger λ , with $\lambda = 0$ specifically coded in deep orange. According to Eq. (5), we divide the color bar of λ into three sections. The one on the left corresponds to $l_{v=-1} = 0$, the one in the middle corresponds to $l_{v=-1} = 1$, and the one on the right corresponds to $l_{v=-1} = 2$. The point with the lowest χ^2 is magnified and the dashed arrow points to its location on the 2D grid of C_6 and C_8 . Panel (b) shows the second step of the search with a much finer grid in the adjacent area of the minimum of the initial search. The three dimensional surface of χ^2 as well as its contours are color coded with the value of χ^2 . Red indicates smaller values while light blue indicates larger values.

$\sigma_{\text{tot}}(E) = \sum_l \sigma_l(E)$, where

$$\sigma_l(E) = \frac{\pi}{k^2} (2l+1) |1 - S|^2 \quad (7)$$

are the partial cross sections and the summation over l is from 0 to infinity. The s -wave partial cross section is related to the s -wave scattering length, $\sigma_{l=0}(E) = 4\pi a_s(E)^2$. Figure 6 shows the total cross section as well as the first five partial cross sections as functions of collision energy. The large peak near 0.04 K comes from a shape resonance in the $l = 3$ channel.

The a_{s0} obtained here is $\sim 50\%$ larger than the previous results determined from interspecies thermalization experiments [43, 44]. The extraction of scattering length from thermalization measurements is sensitive to systematic effects stemming from the determination of absolute

densities and interspecies spatial overlap. While photoassociation spectroscopy together with detailed theoretical analysis as presented in this paper provide more precise values, to gain further confidence in this updated value of the scattering length, we have performed some additional checks as described below.

A. Quantum defect theory predictions

The quantum defect theory (QDT) for $-C_\alpha/R^\alpha$ type of long-range potentials with $\alpha > 2$ [45] provides an analytic connection between the energies of the weakly bound states and the low energy scattering properties through the short-range parameters that are slowly varying functions of energy near the threshold. In particular,

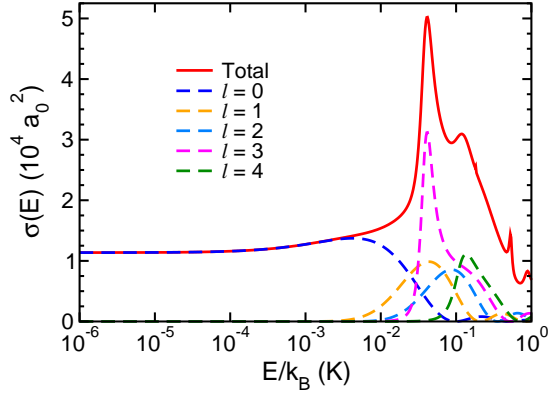


FIG. 6. (color online) The total and first five partial elastic scattering cross sections as functions of collision energy. The solid red line corresponds to the total cross section. The dashed lines corresponds to partial cross sections with $l = 0$ to 4. Note that not all partial wave cross sections that contribute significantly to the total cross section are shown here.

the least bound state energy is related to a_{s0} through the short-range parameter $K_c(E_s, l)$. $E_s = E/s_E$ is the dimensionless scaled energy with the energy scale $s_E = (\hbar^2/2\mu)(1/\beta_6)^2$, where the length scale $\beta_6 = (2\mu C_6/\hbar^2)^{1/4}$. For ${}^6\text{Li}^{174}\text{Yb}$ with $C_6 = 1581.0 E_h/a_0^6$, $\beta_6 = 76.1 a_0$ and $s_E/h = 53.6$ MHz. These two scales are relatively insensitive to the change of C_6 . The s -wave scattering length is related to the zero energy zero partial wave K_c by

$$a_{s0} = \beta_6 \left(b^{2b} \frac{\Gamma(1-b)}{\Gamma(1+b)} \right) \frac{K_c(0,0) + \tan(\pi b/2)}{K_c(0,0) - \tan(\pi b/2)}, \quad (8)$$

where $b = 1/(\alpha - 2)$ with $\alpha = 6$. The least bound state energy is the negative root of the equation

$$\chi_l^c(E_s) = K_c(l, E_s) \quad (9)$$

that is the closest to zero. χ_l^c is a QDT special function defined in Ref. [45]. At $E = -1.8260$ GHz, the least bound state energy corresponds to the scaled energy $E_s = -34.1$. Since K_c varies slowly with energy [45], we can approximate $K_c(0,0)$ with $K_c(E_s, 0)$. Thus, using Eqs. (9) and (8), we get $a_{0s} = 29.2 a_0$, which is consistent with our numerical result above. The slight discrepancy comes from the small energy dependence of the K_c parameter that is mainly due to the effect of the $-C_8/R^8$ term that modifies the long-range wavefunction between the length scale of the $-C_8/R^8$ term and the length scale of the $-C_6/R^6$ term, *i.e.* β_6 . The QDT result confirms that the connection between a_{s0} and the least bound energy is independent of the detailed shape of the short-range potential and the total number of vibrational states it supports.

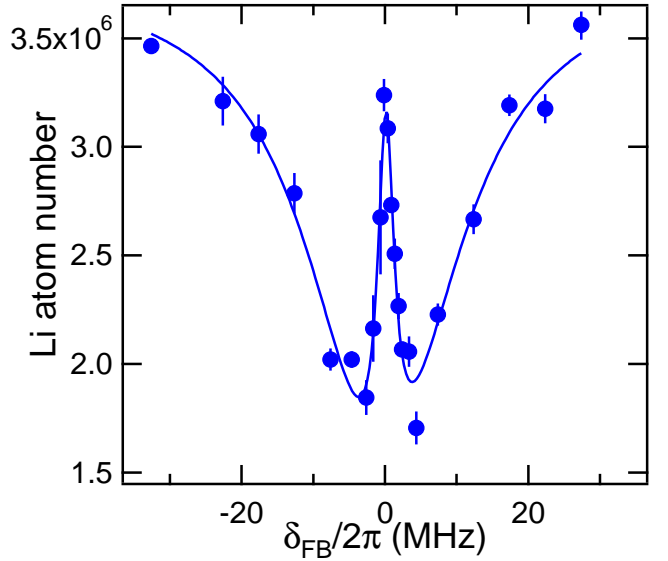


FIG. 7. Representative coherent 2-photon spectrum in which the ground $v = -1$ state is observed as the narrow atom-molecule dark-state feature within a broad loss resonance. For this data, the BB laser was fixed at the $v^* = -2 \leftrightarrow v = -1$ resonance while the FB laser was varied across the $v^* = -2$ 1-photon PA resonance.

V. COHERENT DARK STATE SPECTROSCOPY

In this section, we present our results on the observation of atom-molecule coherence in the YbLi system through coherent two-photon spectroscopy of the least-bound vibrational state $v = -1$. In this scheme, free atom pairs are coupled to this electronic ground molecular state via an excited molecular state with a pair of phase-coherent lasers. This realizes a coherent three-level system where it is well-known that a dark superposition state can be formed [46]. In the context of PA, the dark state is evident in the suppression of PA loss in a frequency range much narrower than the one-photon PA transition itself [47]. The location of this narrow line provides a more precise measurement of the $v = -1$ binding energy. Additionally, our work demonstrates the existence of ground state YbLi molecules in the mixture, and is an important step towards efficient molecule formation using StiRAP from free atoms [48].

To achieve the necessary phase stability between the optical drive fields involved in the coherent two-photon spectroscopy, we modify the experimental setup discussed in Sec II in the following way. We derive the FB and the BB laser beams by splitting the output of a single master diode laser and generating the required frequency difference using AOMs. The ~ 1.8 GHz binding energy of the $v = -1$ state is bridged using the BB (FB) AOM in an upshifted (downshifted) 4-pass orientation [49] and driving both at a frequency ~ 225 MHz using the same direct-digital synthesis (DDS) radiofrequency source.

A representative dark-state spectrum is shown in Figure 7, where a sub-natural linewidth of 2 MHz is observed using the $v^* = -2$ intermediate state. By reducing the BB power and using $v^* = -7$ intermediate state, we have observed linewidths below 400 kHz with reduced strength of the dark resonance feature. Possible causes for the observed linewidth include atom-molecule collisions, spontaneous scattering, and finite temperature effects. The co-existing molecular fraction could be improved in a 3D optical lattice with doublon site filling, where efficient coherent free-bound StiRAP into ground state YbLi molecules may be possible, as has been demonstrated in the homonuclear Sr_2 system [48, 50].

VI. SUMMARY AND OUTLOOK

We have reported our results on two-photon photoassociation spectroscopy of the weakly bound vibrational levels in the electronic ground state of the $^{174}\text{Yb}^6\text{Li}$ molecule. Combining our experimental findings with a detailed theoretical study, we obtained accurate values for the long-range dispersion coefficients for the interatomic potential.

Our work also yields information on Yb-Li scattering properties. We obtained an updated value for the Yb-Li s -wave scattering length of $30a_0$. Furthermore, these

results can refine the predicted locations of magnetic Feshbach resonances in the Yb-Li collisional system [15] [51]. Such resonances characteristic of ground state scattering between alkali and alkaline-earth-like atoms [17] could be used for molecule formation [52].

The observation of coherent atom-molecule dark states in YbLi is an important step towards efficient coherent molecule formation through all-optical methods, possibly in 3D optical lattice confinement [48, 50]. These results together with advances in the related systems of RbYb, RbSr, CsYb [17, 18, 20, 21], provide promise for the realization of a new class of ultracold molecules in the $^2\Sigma^+$ ground state, beyond the bi-alkali paradigm, with applications in quantum simulation and information processing, precision measurements and ultracold chemistry.

VII. ACKNOWLEDGMENTS

We thank Ryan Bowler, Xinxin Tang, and Khang Ton for experimental assistance. Research at University of Washington is supported by NSF Grant No. PHY-1806212 and AFOSR Grant No. FA9550-19-1-0012. Work at Temple University is supported by the ARO Grant No. W911NF-17-1-0563, the AFOSR Grant No. FA9550-14-1-0321, and the NSF Grant No. PHY-1619788.

-
- [1] L. D. Carr, D. DeMille, R. V. Krems, and J. Ye, Cold and ultracold molecules: science, technology, and applications, *New J. Phys.* **11**, 055049 (2009).
 - [2] B. Gadway and B. Yan, Strongly interacting ultracold polar molecules, *J. Phys. B.* **49**, 152002 (2016).
 - [3] T. Zelevinsky, S. Kotochigova, and J. Ye, Precision test of mass-ratio variations with lattice-confined ultracold molecules, *Phys. Rev. Lett.* **100**, 043201 (2008).
 - [4] E. R. Hudson, H. J. Lewandowski, B. C. Sawyer, and J. Ye, Cold molecule spectroscopy for constraining the evolution of the fine structure constant, *Phys. Rev. Lett.* **96**, 143004 (2006).
 - [5] M. Kajita, Prospects for detecting m_e/m_p variance using vibrational transition frequencies of $^2\Sigma$ -state molecules, *Phys. Rev. A* **77**, 012511 (2008).
 - [6] V. V. Flambaum, D. DeMille, and M. G. Kozlov, Time-reversal symmetry violation in molecules induced by nuclear magnetic quadrupole moments, *Phys. Rev. Lett.* **113**, 103003 (2014).
 - [7] J. Hudson, D. Kara, I. Smallman, B. Sauer, M. Tarbutt, and E. Hinds, Improved measurement of the shape of the electron, *Nature* **473**, 493 (2011).
 - [8] V. Andreev, D. G. Ang, D. DeMille, J. M. Doyle, G. Gabrielse, J. Haefner, N. R. Hutzler, Z. Lasner, C. Meisenhelder, B. R. O'Leary, C. D. Panda, A. D. West, E. P. West, and X. Wu, Improved limit on the electric dipole moment of the electron, *Science* **562**, 355 (2018).
 - [9] K.-K. Ni, S. Ospelkaus, M. H. G. de Miranda, A. Pe'er, B. Neyenhuis, J. J. Zirbel, S. Kotochigova, P. S. Julienne, D. S. Jin, and J. Ye, A high phase-space-density gas of polar molecules, *Science* **322**, 231 (2008).
 - [10] T. Takekoshi, L. Reichsöllner, A. Schindewolf, J. M. Hutson, C. R. Le Sueur, O. Dulieu, F. Ferlaino, R. Grimm, and H. C. Nägerl, Ultracold dense samples of dipolar RbCs molecules in the rovibrational and hyperfine ground state, *Phys. Rev. Lett.* **113**, 205301 (2014).
 - [11] P. K. Molony, P. D. Gregory, Z. Ji, B. Lu, M. P. Köppinger, C. R. Le Sueur, C. L. Blackley, J. M. Hutson, and S. L. Cornish, Creation of ultracold $^{87}\text{Rb}^{133}\text{Cs}$ molecules in the rovibrational ground state, *Phys. Rev. Lett.* **113**, 255301 (2014).
 - [12] J. W. Park, S. A. Will, and M. W. Zwierlein, Ultracold dipolar gas of fermionic $^{23}\text{Na}^{40}\text{K}$ molecules in their absolute ground state, *Phys. Rev. Lett.* **114**, 205302 (2015).
 - [13] M. Guo, B. Zhu, B. Lu, X. Ye, F. Wang, R. Vexiau, N. Bouloufa-Maafa, G. Quémener, O. Dulieu, and D. Wang, Creation of an ultracold gas of ground-state dipolar $^{23}\text{Na}^{87}\text{Rb}$ molecules, *Phys. Rev. Lett.* **116**, 205303 (2016).
 - [14] T. M. Rvachov, H. Son, A. T. Sommer, S. Ebadi, J. J. Park, M. W. Zwierlein, W. Ketterle, and A. O. Jamison, Long-lived ultracold molecules with electric and magnetic dipole moments, *Phys. Rev. Lett.* **119**, 143001 (2017).
 - [15] D. A. Brue and J. M. Hutson, Magnetically tunable feshbach resonances in ultracold Li-Yb mixtures, *Phys. Rev. Lett.* **108**, 043201 (2012).
 - [16] W. Dowd, R. Roy, R. Shrestha, A. Petrov, C. Makrides, S. Kotochigova, and S. Gupta, Magnetic field dependent interactions in an ultracold Li-Yb(3P_2) mixture, *New J.*

- Phys. **17**, 055007 (2015).
- [17] V. Barbé, A. Ciamei, B. Pasquiou, L. Reichsöllner, F. Schreck, P. Żuchowski, and J. M. Hutson, Observation of feshbach resonances between alkali and closed-shell atoms, *Nat. Phys.* **14**, 881 (2018).
 - [18] F. Münchow, C. Bruni, M. Madalinski, and A. Görlitz, Two-photon spectroscopy of heteronuclear YbRb, *Phys. Chem. Chem. Phys.* **13**, 18734 (2011).
 - [19] R. Roy, R. Shrestha, A. Green, S. Gupta, M. Li, S. Kotochigova, A. Petrov, and C. H. Yuen, Photoassociative production of ultracold heteronuclear YbLi* molecules, *Phys. Rev. A* **94**, 033413 (2016).
 - [20] A. Ciamei, J. Szczepkowski, A. Bayerle, V. Barbé, L. Reichsöllner, S. M. Tzanova, C. C. Chen, B. Pasquiou, A. Grochola, P. Kowalczyk, W. Jastrzebski, and F. Schreck, The RbSr $^2\Sigma^+$ ground state investigated via spectroscopy of hot and ultracold molecules, *Phys. Chem. Chem. Phys.* **20**, 26221 (2018).
 - [21] A. Guttridge, M. D. Frye, B. C. Yang, J. M. Hutson, and S. L. Cornish, Two-photon photoassociation spectroscopy of CsYb: Ground-state interaction potential and interspecies scattering lengths, *Phys. Rev. A* **98**, 022707 (2018).
 - [22] A. Micheli, G. K. Brennen, and P. Zoller, A toolbox for lattice-spin models with polar molecules, *Nat. Phys.* **2**, 341 (2006).
 - [23] K. M. Jones, E. Tiesinga, P. D. Lett, and P. S. Julienne, Ultracold photoassociation spectroscopy: Long-range molecules and atomic scattering, *Rev. Mod. Phys.* **78**, 483 (2006).
 - [24] We will present our spectroscopy of this excited molecular state, which extends our previous observations in [19], in a future publication.
 - [25] R. Roy, A. Green, R. Bowler, and S. Gupta, Two-element mixture of Bose and Fermi superfluids, *Phys. Rev. Lett.* **118**, 055301 (2017).
 - [26] E. R. I. Abraham, N. W. M. Ritchie, M. W. I., and R. G. Hulet, Photoassociative spectroscopy of longrange states of ultracold $^6\text{Li}_2$ and $^7\text{Li}_2$, *J. Chem. Phys.* **103**, 7773 (1995).
 - [27] R. J. LeRoy, and R. B. Bernstein, Dissociation energy and long-range potential of diatomic molecules from vibrational spacings at higher levels, *J. Chem. Phys.* **52**, 3869 (2006).
 - [28] R. Roy, R. Shrestha, A. Green, S. Gupta, M. Li, S. Kotochigova, A. Petrov, and C. H. Yuen, Photoassociative production of ultracold heteronuclear YbLi* molecules, *Phys. Rev. A* **94**, 033413 (2016).
 - [29] Deeper bound states ($v = -7$ and lower) were inaccessible in this work due to the choice of laser diodes used for PA. Future work can expand on the current study by using laser diodes centered at longer wavelengths.
 - [30] K. T. Tang and J. P. Toennies, An improved simple model for the van der Waals potential based on universal damping functions for the dispersion coefficients, *J. Chem. Phys.* **80**, 3726 (1984).
 - [31] P. Zhang, H. R. Sadeghpour, and A. Dalgarno, Structure and spectroscopy of ground and excited states of LiYb, *J. Chem. Phys.* **133**, 044306 (2010).
 - [32] D. A. Brue and J. M. Hutson, Prospects of forming ultracold molecules in $^2\Sigma$ states by magnetoassociation of alkali-metal atoms with Yb, *Phys. Rev. A* **87**, 052709 (2013).
 - [33] M. S. Safronova, S. G. Porsev, and C. W. Clark, Ytterbium in quantum gases and atomic clocks: van der waals interactions and blackbody shifts, *Phys. Rev. Lett.* **109**, 230802 (2012).
 - [34] S. G. Porsev, M. S. Safronova, A. Derevianko, and C. W. Clark, Relativistic many-body calculations of van der Waals coefficients for Yb-Li and Yb-Rb dimers, *Phys. Rev. A* **89**, 022703 (2014).
 - [35] A. J. Thakkar and V. H. Smith, Mist: A new interatomic potential function, *Chem. Phys. Lett.* **24**, 157 (1974).
 - [36] G. Gopakumar, M. Abe, B. P. Das, M. Hada, and K. Hirao, Relativistic calculations of ground and excited states of LiYb molecule for ultracold photoassociation spectroscopy studies, *J. Chem. Phys.* **133**, 124317 (2010).
 - [37] S. Kotochigova, A. Petrov, M. Linnik, J. Kos, and P. S. Julienne, *Ab initio* properties of Li-group-II molecules for ultracold matter studies, *J. Chem. Phys.* **135**, 164108 (2011).
 - [38] S. N. Tohme, M. Korek, and R. Awad, *Ab initio* calculations of the electronic structure of the low-lying states for the ultracold LiYb molecule, *J. Chem. Phys.* **142**, 114312 (2015).
 - [39] We neglect small effects such as couplings between the rotational angular momentum of the diatom and the spins, including the nuclear and the electronic ones, and the dependence on the nuclear separation R of the hyperfine constant and the g -factors. Thus the spins are completely decoupled from the nuclear motion, and the hyperfine splittings of the molecular bound states in a magnetic field is the same as the ones in the separate-atoms limit.
 - [40] P. J. Mohr and B. N. Taylor, CODATA recommended values of the fundamental physical constants: 1998, *Rev. Mod. Phys.* **72**, 351 (2000).
 - [41] Although l_v are used as unknown variables, they are discrete and remain zero in the vicinity of the minimum where the error propagation is practically done. Therefore we don't count them as variables in the error analysis.
 - [42] R. G. Gordon, New method for constructing wavefunctions for bound states and scattering, *J. Chem. Phys.* **51**, 14 (1969).
 - [43] V. V. Ivanov, A. Khramov, A. H. Hansen, W. H. Dowd, F. Münchow, A. O. Jamison, and S. Gupta, Sympathetic cooling in an optically trapped mixture of alkali and spin-singlet atoms, *Phys. Rev. Lett.* **106**, 153201 (2011).
 - [44] H. Hara, Y. Takasu, Y. Yamaoka, J. M. Doyle, and Y. Takahashi, Quantum degenerate mixtures of alkali and alkaline-earth-like atoms, *Phys. Rev. Lett.* **106**, 205304 (2011).
 - [45] B. Gao, General form of the quantum-defect theory for $-1/r^\alpha$ type of potentials with $\alpha > 2$, *Phys. Rev. A* **78**, 012702 (2008).
 - [46] S. E. Harris, Electromagnetically induced transparency, *Physics Today* **50**, 36 (1997).
 - [47] K. Winkler, G. Thalhammer, M. Theis, H. Ritsch, R. Grimm, and J. H. Denschlag, Atom-molecule dark states in a Bose-Einstein condensate, *Phys. Rev. Lett.* **95**, 063202 (2005).
 - [48] S. Stellmer, B. Pasquiou, R. Grimm, and F. Schreck, Creation of ultracold Sr_2 molecules in the electronic ground state, *Phys. Rev. Lett.* **109**, 115302 (2012).
 - [49] B. Lu and D. Wang, Note: A four-pass acousto-optic modulator system for laser cooling of sodium atoms, *Rev. Sci. Instr.* **88**, 076105 (2017).

- [50] A. Ciamei, A. Bayerle, C. C. Chen, B. Pasquiou, and F. Schreck, Efficient production of long-lived ultracold Sr_2 molecules, *Phys. Rev. A* **96**, 013406 (2017).
- [51] We have recently observed magnetic Feshbach resonances in Yb-Li at locations consistent with predictions based on the work presented in this paper. These observations will be reported in a forthcoming publication.
- [52] M. Mark, F. Meinert, K. Lauber, and H. Nägerl, Mott-insulator-aided detection of ultra-narrow feshbach resonances, *SciPost Phys.* **5**, 055 (2018).